In-situ synthesis of Fe-Mn-Si-Cr-Ni shape memory alloy functional coating by laser cladding

Peng Xu (徐 鹏), Heng Ju (鞠 恒), Chengxin Lin (林成新)*, Chaoyu Zhou (周超玉), and Dewei Pan (潘德位)

Transportation Equipment and Ocean Engineering College, Dalian Maritime University, Dalian 116026, China

**Corresponding author: lchxin@dlmu.edu.cn*

Received December 19, 2013; accepted February 12, 2014; posted online April 4, 2014

Fe-Mn-Si-Cr-Ni composite powders are utilized to form a functional shape memory alloy cladding layer (SMACL) using a laser cladding method. The microstructure, microhardness, and phase composition of the SMACL are measured, and the extent of deformation of the laser cladding samples is determined. The SMACL is composed of planar, cellular, and dendritic crystals, equiaxed grains, and oxides with increasing distance from the substrate surface. The SMACL is further composed of ε-martensite and γ-austenite phases, while the tempered SMACL consists mainly of γ-austenite. Extensive deformation occurs in AISI 304 stainless steel laser cladding samples. By contrast, limited deformation is observed in the SMACL samples.

OCIS codes: 140.3390, 160.3900, 350.3850.

doi: 10.3788/COL201412.041403.

Laser cladding has recently attracted research attention because of its unique properties, which include wear resistance, corrosion resistance, and metallurgical bonding between the coating and the substrate[1,2]. However, the laser cladding technique also presents several disadvantages; for example, the thermal stress that develops during the laser cladding process can lead to crack formation in composite coatings[3]. Several methods have been suggested to reduce the crack sensitivity of laser cladded layer; these methods include preheating of the substrate, addition of a transition zone, optimization of the processing parameters, or addition of a plastic phase in the clad coating[4–6]. However, these approaches require complicated technology at a high cost.

Since the shape memory effect (SME) in Fe-Mn-Si alloys was firstly discovered by Saito *et al.* in 1982, these low-cost alloys have gained much attention because of their favorable workability and machinability[7,8]. The SME in Fe-Mn-Si-based alloys originates from the reversion of non-thermoelastic stress-induced ε-martensite, also called stress-induced ε-martensite transformation; its reverse transformation and its transformation deformation can adapt to the change of external macroscopic stress under the outside stress[9]. This so-called stress self-accommodation characteristic of Fe-Mn-Si-based shape memory alloys can be used in specific fields, such as in laser cladding[10,11].

In this letter, an Fe17Mn5Si10Cr3Ni shape memory alloy coating is prepared on an AISI 304 stainless steel surface by laser cladding using the presetting powder method. The cladding powders are designed independently. The loss ratios of Fe, Mn, Si, Cr, and Ni during the laser cladding process are then detected and analyzed, and the microstructure, microhardness, and phase constitution of the cladding layer are investigated.

AISI 304 stainless steel with dimensions of 50×100×10 (mm) was used as the substrate material. After processing by finish turning, the substrate was burnished using fine emery paper and then rinsed with acetone before laser cladding. The particle sizes of Fe, Mn, Si, Cr, and Ni powders ranged from 10 to 50 μm, and the purity of these powders was at least 99.9%. Fe/Mn/Si/Cr/Ni powder blends were evenly mixed in air using a dry ball mill for about 4 h. The blends were then placed in a vacuum drying oven, pre-heated at 300 °C for 1 h, and uniformly placed on AISI 304 stainless steel (chemical composition wt.%: C 0.043, Mn 0.93, Si 0.33, Cr 17.32, Ni 8.03, Fe bal.) to form a loose layer approximately 1-mm thick. A continuous wave (CW) CO_2 laser of 10.6-μm wavelength (5-kW maximum power) was utilized for material processing. Laser processing was conducted at 2-kW power with a 3-mm laser spot diameter, 800-mm/min scanning speed, and 50% overlap rate.

Chemical constituents were tested by a multi-channel spark direct reading spectrometer (QSN750). Microstructures were studied by an OLYMPUS GX51 optical microscope using samples prepared by standard mechanical grinding/polishing and etching with aqua regia for 5–10 s. The phase composition of the cladding layer was determined by X-ray diffractometry (XRD) using a Rigaku diffractometer operated in Bragg–Brentano geometry with Cu Kα radiation. The chemical composition of the layer was detected using an energy dispersive spectrometer (EDS) equipped with a scanning electron microscope; here, the acceleration voltage was 10 kV. The microhardness of the coatings was measured using a MH-6 semi-automatic hardness tester. The microhardness profile was obtained from the cross-section of the cladding sample at distances of every 100 μm from the coating surface to the substrate. A 100-g testing load and a 5-s load dwelling time were used to measure the average hardness. Measurements were repeated thrice, and the average value of these measurements was obtained.

Figure 1 shows the surface morphology and XRD patterns of the Fe-Mn-Si-Cr-Ni SMACL. Figure 1(a) shows the smooth surface morphology of SMACL produced under proper technical conditions (i.e., 2-kW power, 3-mm laser spot diameter, 800-mm/min scanning speed, and 50% overlap rate). Black precipitates and gray ox-

ide coatings form on the surface of the resultant layer (Fig. 1(a)). After laser cladding, some parts of the precipitates and oxide coatings peel off with decreasing cladding layer temperature. EDS analysis shows that the black precipitates contain C 4.31 wt.-%, O 32.89 wt.-%, Si 7.48 wt.-%, and Mn 54.46 wt.-% (atomic percentages: C 9.7%, O 55.49%, Si 7.19%, and Mn 26.76%). Mn and Si react with O_2 to form oxides during the heating and cooling progress; thus, SiO_2 and MnO_x are present in the black precipitates. MnSi, SiC, and monoatomic carbon also appear to exist in the layer. The gray oxide coating is composed of C 6.85 wt.-%, O 31.69 wt.-%, Mn 9.92 wt.-%, and Fe 50.61 wt.-% (atomic percentages: C 15.52%, O 53.96%, Mn 4.92%, and Fe 24.69%). Thus, FeO_x and MnO_x are present in the gray oxide coatings. FeC_3 and monoatomic carbon may also be present in the coating.

The chemical composition of the SMACL with the black precipitates and gray oxide coating is Fe 61.85 wt.-%, Mn 17.66 wt.-%, Si 4.89 wt.-%, Cr 10.56 wt.-%, and Ni 5.31 wt.-%. These values are similar to those found in Fe17Mn5Si10Cr3Ni SMA. The XRD pattern of the Fe-Mn-Si-Cr-Ni SMACL is shown in Fig. 1(c). The SMACL is composed of austenite (γ) and martensite (ε). The ε phase of the SMACL forms from the transformation of γ to remove residual stress that forms during the laser cladding process. Figure 1(b) displays the smooth and glossy surface morphology of the SMACL after tempering at 1000 °C for 1 h; Fig. 1(d) shows the corresponding XRD pattern of the layer. The tempered SMACL consists of γ, which is attributed to the $\varepsilon \rightarrow \gamma$ phase transformation in Fe-Mn-Si SMA.

Figure 2 depicts the microhardness profiles of the SMACL obtained every 100 μm from the coating surface to the substrate. The microhardness of the heat-affected zone (HAZ) and substrate is approximately Hv220. The SMACL has an average hardness of approximately Hv263, which is higher than that of AISI 304 stainless steel. This result may be attributed to solution strength and precipitation hardening effects.

The defect-free microstructure of the Fe-Mn-Si-Cr-Ni SMACL produced by multi-track overlapping laser cladding is shown in Fig. 3(a). Figure 3(b) shows a schematic diagram of the SMACL based on our observation. The binder metal undergoes planar growth at the bottom of the coating. Cellular and dendritic structures may be observed with increasing distance from the substrate surface; equiaxed grains also appear above these structures, which is in accordance with previous research[12,13]. A layer of Mn, Fe, and Si oxides is found at the apex of the cladding layer. The heat source of the laser beam has a Gaussian distribution and laser spot geometry; in addition, the laser displacement induces non-uniform temperatures in the melting bath[14,15]. A perturbed thermal field leads to various thermal gradients and cooling rates. According to solidification theory, the growth morphology of a solidification structure is determined by the stabilization factor between solid and liquid interfaces (i.e., G/R, where G is the temperature gradient and R is the solidification rate). During the heating and cooling process, each region of the cladding layer shows different microstructures attributable to different cooling rates. Figures 3(c) and (d) respectively show the microstructure of the tempered SMACL and its schematic diagram. The ε-martensite in the cladding layer is completely transformed into γ-austenite during tempering. On average, the γ-austenite in the cladding layer is approximately 100-μm thick, whereas the substrate is about 45-μm thick. This phenomenon is believed to be caused by the high temperature of the molten pool during the laser cladding process.

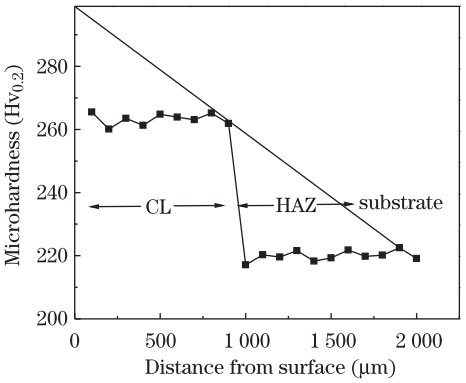

Fig. 2. SMACL microhardness.

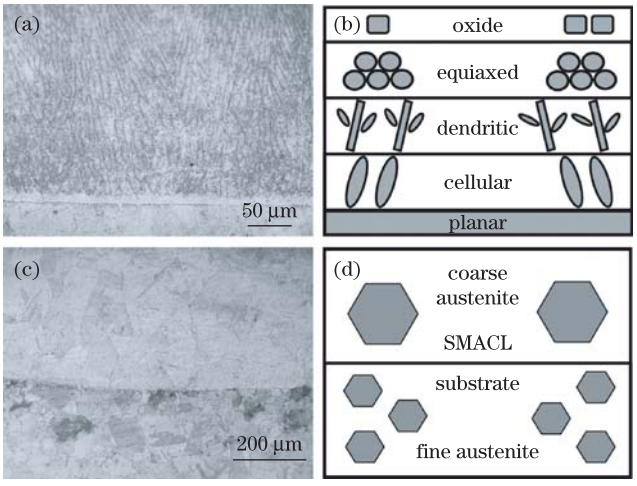

Fig. 3. (a) Microstructure and (b) schematic diagram of the Fe-Mn-Si-Cr-Ni SMACL; (c) microstructure and (d) schematic diagram of the tempered SMACL.

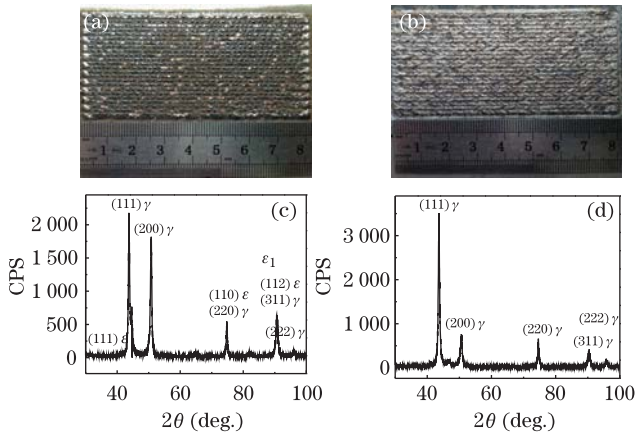

Fig. 1. (a) Surface morphology and (c) XRD patterns of the Fe-Mn-Si-Cr-Ni SMACL; (b) surface morphology and (d) XRD patterns of the tempered SMACL.

Stresses generated during the laser cladding process are a fundamental concern. The high thermal gradients produced by the lasing process and mismatches in material properties may result in the development of significant stresses within the material. These tensile residual stresses may arise in the clad and cause cracking within the clad and/or within the substrate, which, in turn, results in poor mechanical performance (such as fatigue strength or resistance to stress corrosion) and dimensional stability (i.e., distortion) of the base material deposited. Figure 4 shows the extent of deformation of the two types of substrates. Figure 4(a) demonstrates that deformation occurs in the AISI 304 stainless steel laser cladding samples. This type of distortion induced by residual stresses may be decreased or eliminated by various approaches, such as processing parameter optimization, interlayer construction to minimize thermal mismatches between the clad and the substrate, substrate preheating during cladding, and performing post-cladding stress-relieving treatments. Figure 4(b) shows slight deformation in the SMACL samples. The extent of deformation is known to reflect the intensity of residual stresses. $\gamma \rightarrow \varepsilon$ phase transformation that releases residual stresses in Fe-Mn-Si SMA is responsible for the slight distortions observed.

In conclusion, an Fe-Mn-Si-Cr-Ni shape memory alloy functional coating is synthesized through laser cladding of Fe/Mn/Si/Cr/Ni powder blends. The SMACL microstructure contains planar, cellular, and dendritic crystals, equiaxed grains, and oxides with increasing distance from the substrate surface. The SMACL is composed of ε-martensite and γ-austenite, whereas the tempered SMACL consists of γ-austenite. This phenomenon demonstrates that γ-austenite$\rightarrow$ ε-martensite transformation occurs during laser processing. The SMACL releases residual stresses, which is the driving force of the $\gamma \rightarrow \varepsilon$ phase transformation.

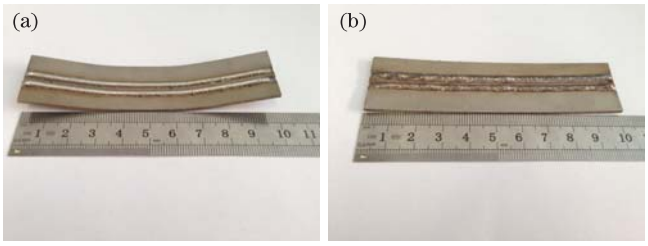

Fig. 4. Extent of deformation of the substrates. (a) AISI 304 stainless steel cladding layer and (b) SMACL.

This work was supported by the Research Fund for the Doctoral Program of Higher Education of China (No. 20122125120013), the Dalian Science and Technology Fund (No. 2011J21DW003), and the Fundamental Research Funds for the Central Universities (Nos. 3132013060 and 3132013311).

References

1. C. Gou, D. Shen, J. Long, and F. Wang, Chin. Opt. Lett. **10,** 091406 (2012).
2. Y. Huang, Y. Yang, G. Wei, W. Shi, and Y. Li, Chin. Opt. Lett. **6,** 356 (2008).
3. I. Shishkovsky and I. Smurov, Mater. Lett. **73,** 32 (2012).
4. H. Köhler, K. Partes, J. R. Kornmeier, and F. Vollertsen, Phys. Procedia. **39,** 354 (2012).
5. A. Suárez, J. M. Amado, M. J. Tobar, A. Yáñez, E. Fraga, and M. J. Peel, Surf. Coat. Technol. **204,** 1983 (2010).
6. M. M. Alam, J. Karlsson, and A. F. H. Kaplan, Mater. Design **32,** 1814 (2011).
7. T. Saito, C. Kapusta, and A. Takasaki, Mat. Sci. Eng. A-Struct. **592,** 88 (2014).
8. S. N. Balo and F. Yakuphanoglu, Thermochim. Acta. **560,** 43 (2013).
9. N. V. Caenegem, L. Duprez, K. Verbeken, D. Segers, and Y. Houbaert, Mat. Sci. Eng. A-Struct. **481-482,** 183 (2008).
10. H. Lee, H. J. Koh, C. H. Seo, and N. J. Kim, Scripta Mater. **59,** 83 (2008)
11. B. Liu, Y. F. Zheng, and L. Q. Ruan, Mater. Lett. **65,** 540 (2011).
12. D. Xie, J. Zhao, Y. Qi, Y. Li, L. Shen, and M. Xiao, Chin. Opt. Lett. **11,** 111401 (2013).
13. W. Qiu and J. Wang, Chin. Opt. Lett. **10,** 041601 (2012).
14. M. Z. Hao and Y. W. Sun, Int. J. Heat Mass Tran. **64,** 352 (2013).
15. Q. Zhang, J. Yao, P. Wang, J. Zhou, Y. Xia and B. Zhang, Chin. Opt. Lett. **2,** 468 (2004).